

# Dirac magnons, nodal lines, and nodal plane in elemental gadolinium

A. Scheie,<sup>1,\*</sup> Pontus Laurell,<sup>2,3,†</sup> G. E. Granroth,<sup>1</sup> M. B. Stone,<sup>1</sup> and S. E. Nagler<sup>1,4</sup>

<sup>1</sup>Neutron Scattering Division, Oak Ridge National Laboratory, Oak Ridge, TN 37831, USA

<sup>2</sup>Computational Sciences and Engineering Division, Oak Ridge National Laboratory, Oak Ridge, TN 37831, USA

<sup>3</sup>Department of Physics and Astronomy, University of Tennessee, Knoxville, TN 37996, USA.

<sup>4</sup>Quantum Science Center, Oak Ridge National Laboratory, Tennessee 37831, USA

(Dated: July 27, 2021)

We investigate the magnetic excitations of elemental gadolinium (Gd) using inelastic neutron scattering, showing that Gd is a Dirac magnon material with nodal lines at  $K$  and nodal planes at half integer  $\ell$ . We find an anisotropic intensity winding around the  $K$ -point Dirac magnon cone, which is interpreted to indicate Berry phase physics. Using linear spin wave theory calculations, we show the nodal lines have non-trivial Berry phases, and topological surface modes. Together, these results indicate a highly nontrivial topology, which is generic to hexagonal close packed ferromagnets. We discuss potential implications for other such systems.

Topological materials exhibiting quasiparticles with linear band crossings effectively described by the Dirac equation play an important role at the frontier of condensed matter physics [1, 2]. The electronic structure of Graphene established it as the prototypical example of a fermionic Dirac material [1, 3]. It was subsequently realized that related physics can occur in systems with bosonic quasiparticles including among others phonons [4], photons [5, 6], and more recently, magnons [7–12]. The interesting topological features of magnon bands are often associated with band degeneracies that can be understood as a consequence of symmetries describable by spin-space groups [13, 14]. Magnon band structures can realize analogs of e.g. Chern insulators and topological semimetals [10–12] and can host both Dirac [7, 8, 15] or Weyl magnons [16–20], as well as exhibit extended nodal degeneracies [15, 21, 22] and triply-degenerate points [23]. Consequently magnetic systems can also exhibit phenomena similar to those found in topological electronic materials, for example a magnon thermal Hall effect arising from gapped bands with topologically non-trivial Chern numbers [24–29].

Dirac band crossings have been observed in the layered local-moment magnetic systems  $\text{CrI}_3$  [30] and  $\text{CoTiO}_3$  [31, 32]. These systems are related to the honeycomb ferromagnet, a simple bipartite lattice that is the prototypical example of a two-dimensional Dirac magnon system. One strong indicator of non-trivial topology is an anisotropic “winding” intensity around the Dirac point topology, as seen in  $\text{CoTiO}_3$  [33, 34]. Dirac magnons have also been observed in the three-dimensional antiferromagnet  $\text{Cu}_3\text{TeO}_6$  [35, 36].

In this Letter we use inelastic neutron scattering to measure the magnon spectrum of elemental gadolinium (Gd), showing directly that it is a Dirac material. Gd is a highly isotropic ferromagnet with the hexagonal close packed (HCP) structure that forms a simple three-dimensional bipartite lattice. We demonstrate experimentally that the magnon bands in Gd exhibit Dirac nodal lines with a clear anisotropic winding intensity, and interestingly also show a nodal plane. A calculation using spin-wave theory confirms that the nodal lines have a non-trivial Berry phase, and give rise to topological surface modes. The results suggest that the entire class of rare earth

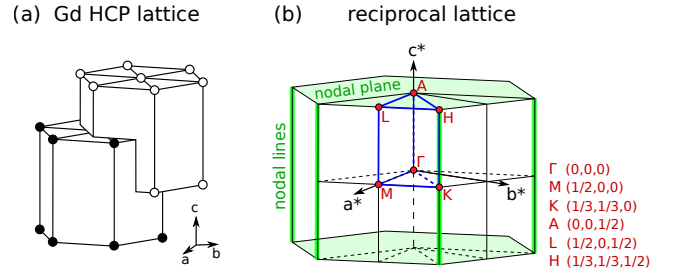


Figure 1. (a) HCP crystal structure of Gd. The lattice is bipartite, with interpenetrating layers of ABAB-stacked triangular lattices. (b) First Brillouin zone of Gd. The dark blue lines delineate the asymmetric unit in reciprocal space, the red dots show the high symmetry points (notated on the right), and the green regions indicate nodal lines at  $h = k = 1/3$  and nodal planes at  $\ell = \pm 1/2$ .

HCP ferromagnets is a simple model system for topological magnetism.

The Gd HCP structure and its reciprocal lattice are illustrated in Fig. 1. Gd orders ferromagnetically at  $T_c = 293$  K [37–39]. Although Gd is metallic, the first three valence electrons are completely itinerant and the rest are localized, leaving an effective  $\text{Gd}^{3+}$  at each site [40]. In the half-filled  $f$  shell, the orbital angular momentum is effectively quenched leaving  $S = 7/2$  magnetism [41] with near-perfect isotropy and spin-orbit coupling that vanishes to first order. (Small anisotropies do exist in Gd [42] which influence the direction of the ordered moment [38], but these are of the order  $30 \mu\text{eV}$  [43]—so small that they have never been measured with neutrons.) This makes Gd an ideal material for studying Heisenberg exchange on a hexagonal lattice.

The Gd spin wave spectrum was first measured by Koehler et al. in 1970 [44]; but only along  $(hh0)$ ,  $(h\bar{h}0)$ ,  $(h00)$ , and  $(00\ell)$  directions. These data show a linear magnon band crossing at  $K = (1/3, 1/3, 0)$ , indicating a Dirac node and suggesting the possibility of nontrivial topology. The temperature dependence of the Gd magnons was measured in the 1980’s [45, 46], but only along the same symmetry directions as Ref. [44]. Here we have used SEQUOIA, a modern time of flight spectrometer [47, 48] at the SNS [49], to measure the Gd in-

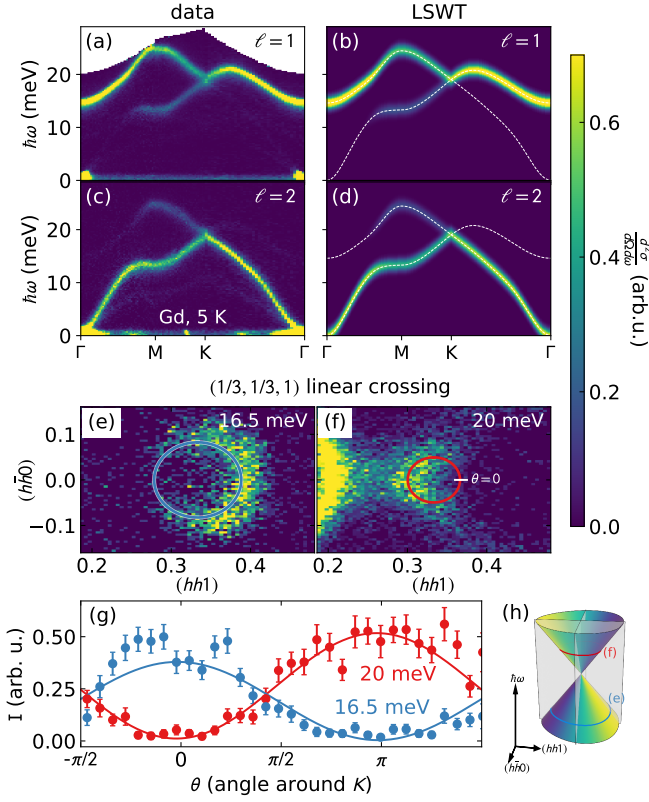


Figure 2. Measured and fitted spin wave spectra of Gd. Panels (a) and (c) show the measured Gd spectra along high-symmetry directions. Panels (b) and (d) show spin wave theory calculated spectra using the best fit Hamiltonian [52]. The top row shows the scattering at  $\ell = 1$ , the second row at  $\ell = 2$ . Note the linear band crossing at  $K$ . Panels (e) and (f) show constant energy slices above and below the band crossing, showing “intensity arcs”. Panel (g) shows the intensity binned around the circles in (e) and (f), fitted to a sin function. (h) The “Dirac node” dispersion surface, with colored circles indicating the slices in panels (e)-(f).

elastic neutron spectrum over the entire Brillouin zone volume. The sample was a 12 g isotopically enriched  $^{160}\text{Gd}$  single crystal (in fact, the same crystal as was used in Ref. [44]) aligned with the  $hh\ell$  plane horizontal. Measurements were carried out at 5 K with incident energies  $E_i = 50$  meV and 100 meV. Data were processed with *Mantid* software [50]; see the Supplemental Materials [51] and Ref. [52] for further details. The resulting full data set allows one to directly see topological features in the spectrum. The data were thoroughly analyzed to determine an accurate spin exchange Hamiltonian: this is discussed in detail in a separate paper [52] focusing on the Gd magnetic interactions. Here we focus on the topological properties of the Gd magnon bands, showing the existence of a Dirac magnon at  $K$ , and nodal planes at half-integer  $\ell$ .

Data along high-symmetry directions are shown in Fig. 2 alongside the LSWT fit. As this comparison demonstrates, the refined model closely reproduces the measured spectrum. Due to this agreement and the high spin length ( $S = 7/2$ ), LSWT provides a good description of Gd.

From a topology perspective, there are two particularly noteworthy features in the Gd scattering: a nodal line degeneracy at  $h = k = 1/3$  extending along  $\ell$ , and a nodal plane degeneracy at  $\ell = 1/2$ . We will discuss each in turn.

The first feature in the data is a linear band crossing at  $K$ , shown in Fig. 2. As shown in Fig. 3, it extends along  $\ell$ , making it a nodal line. This band crossing shows an anisotropic intensity pattern [Fig. 2 (e)-(h)], where the intensity follows sinusoidal modulation winding around the Dirac cone, inverted above and below the crossing point. A similar intensity winding was seen in  $\text{CoTiO}_3$  [31, 32], and is understood to be a signature of the nodal line and nontrivial Berry phase around  $(1/3, 1/3, \ell)$  [33, 34]. (This is similar to a signature of Berry phase physics in graphene seen using polarization-dependent angle-resolved photoemission spectroscopy [53].) Unlike  $\text{CoTiO}_3$ , the offset angle of the intensity winding is zero to within error bars: no anisotropy or off-diagonal exchange shifts the intensity away from the  $(hh0)$  line.

To more firmly establish the topological nature of the nodal line, we turn to linear spin-wave theory [54, 55]. Rather than using the full fitted Gd Hamiltonian [52], we here use a simplified  $J_1 - J_2 - J_3$  model that qualitatively captures the main features of the full fitted model, including the band crossings,

$$H = J_1 \sum_{\langle i,j \rangle} \mathbf{S}_i \cdot \mathbf{S}_j + J_2 \sum_{\langle\langle i,j \rangle\rangle} \mathbf{S}_i \cdot \mathbf{S}_j + J_3 \sum_{\langle\langle\langle i,j \rangle\rangle\rangle} \mathbf{S}_i \cdot \mathbf{S}_j, \quad (1)$$

where  $J_n$  represents  $n$ th nearest neighbor exchange. (For the values of the exchange couplings, see Ref. [52].)  $J_1$  and  $J_3$  couple the two sublattices, whereas  $J_2$  couple only sites within the same sublattice (within  $ab$ -planes).  $J_n < 0$  ( $J_n > 0$ ) indicates ferromagnetic (antiferromagnetic) exchange. The simplified model makes analytical LSWT calculations feasible. Details of these calculations are shown in the Supplemental Material [51]. This model includes three of the four largest magnitude exchange interactions that were determined in the full fit. (Here we exclude  $J_4 \approx J_3$ , where  $J_4$  couples sites along  $\hat{c}$ . Since  $J_4$  has a lower coordination number than  $J_{1,2,3}$ , it only produces a smaller  $\ell$ -dependent contribution to the energy. The exclusion of  $J_4$  does not affect the topology [51], but will enable clearer plots of surface modes.) We find the two magnon modes to have energies  $\epsilon_{1,2} = \epsilon_0(\mathbf{k}) \pm \Delta\epsilon(\mathbf{k})$ , where  $\epsilon_0(\mathbf{k}) = -12S(J_1 + J_2 + J_3) + 12SJ_2\gamma_2(\mathbf{k})$ , and the gap  $2\Delta\epsilon(\mathbf{k}) = 24S|J_1\gamma_1(\mathbf{k}) + J_3\gamma_3(\mathbf{k})|$  depends only on the inter-sublattice interactions  $J_{1,3}$ . We have used  $\gamma_n(\mathbf{k}) = \frac{1}{z_n} \sum_{\vec{\delta}_n} e^{-i\mathbf{k}\cdot\vec{\delta}_n}$ , where  $z_n$  is the number of  $n$ th nearest neighbors, and  $\vec{\delta}_n$  are the  $n$ th nearest neighbor vectors. Non-accidental degeneracies thus correspond to  $\gamma_1(\mathbf{k}) = \gamma_3(\mathbf{k}) = 0$ , which only occur at the nodal plane and lines.

The HCP lattice is inversion symmetric, and the spin-wave Hamiltonian has an effective time-reversal symmetry [17]. Together, these symmetries guarantee that the Berry curvature vanishes everywhere, and thus HCP Gd does not have non-trivial Chern numbers or Weyl magnons. Nevertheless, the system is far from trivial. The topology of the magnon nodal

lines can be classified in terms of the Berry phase

$$\gamma_m [C] = \oint_C d\mathbf{k} \cdot \mathcal{A}_m(\mathbf{k}), \quad (2)$$

where  $C$  is a closed contour,  $\mathcal{A}_m = i \langle u_m(\mathbf{k}) | \nabla_{\mathbf{k}} | u_m(\mathbf{k}) \rangle$  is the Berry connection, and  $|u_m(\mathbf{k})\rangle$  is the  $m$ th energy eigenstate of the magnon Hamiltonian. If the contour  $C$  is pierced once by a nodal line, it is trivial if  $\gamma_m = 0$  and non-trivial if  $\gamma_m = \pi$ . Direct evaluation for Eq. (S1) for Gd shows  $\gamma_m [C] = \pm\pi$  for contours surrounding the nodal lines at  $K$  and  $K'$  [51], thus demonstrating their topological nature.

A second noteworthy feature is a nodal plane. As shown in Fig. 3, the Dirac cone flattens and then inverts as  $\ell$  increases (plotting between  $\ell = 1$  and  $\ell = 2$ —the cone at  $\ell = 0$  is not fully visible due to kinematic constraints of the experiment). In fact, every integer shift in  $\ell$  brings an inversion in the Dirac cone intensity, and every half-integer  $\ell$  gives a degeneracy in the modes at all  $h$  and  $k$ . This degeneracy, shown in Fig. 3(e) and (f) where the Dirac cone is completely flattened, gives rise to a nodal plane. There is not yet an established topological classification of magnon nodal planes (or more generally, surfaces), but we note that the nodal plane in Gd is not topologically charged in the  $(\mathbb{Z})$  sense of Ref. [56]. In that approach, the total Berry curvature is integrated over two planes surrounding the nodal plane, and used to define an integer-valued topological invariant. Since the Berry curvature vanishes everywhere in our model, we conclude the nodal plane in Gd is topologically trivial in this sense. A potential alternative way to classify the nodal plane would be using a  $\mathbb{Z}_2$  invariant, as is used in topological insulators. We note that Ref. [57] introduced a  $\mathbb{Z}_2$  invariant for electronic nodal surfaces, and we look forward to the future development of a similar invariant for magnon systems.

The nodal plane's topological classification notwithstanding, it should be noted that neither of these degeneracies—the nodal line at  $h = k = 1/3$  and the nodal plane at  $\ell = 1/2$ —depend sensitively upon the details of the magnetic exchange Hamiltonian. On the HCP lattice, they appear with both the simplest single nearest neighbor ferromagnetic exchange interaction, or with any number of further neighbor exchanges—so long as they are all Heisenberg exchanges and the ground state remains ferromagnetic (this was first noted by Brinkman in 1967 [13] and the topological consequences have been explored in Ref. [14]). Thus, although the further neighbor exchange interactions are important for understanding the wiggles in Gd's magnon dispersion, they are not important for understanding the topology.

Some of the more interesting consequences of band topology are found in the surface magnon modes. To investigate this, we theoretically considered the simplest geometry for surface modes: a slab of a finite number triangular lattice layers along  $\hat{c}$  as shown in Fig. 1. This was done for the full fitted LSWT model (30 neighbor exchange terms) using the *SpinW* software [58] by creating a supercell geometry with and without periodic boundary conditions in the  $c$  direction (the  $c$  termination was generated by creating a blank space at the top

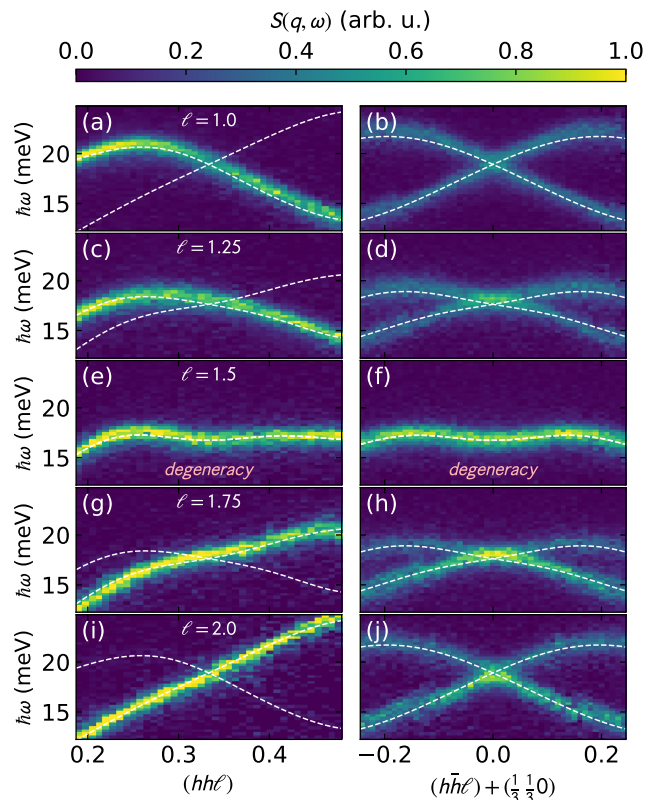


Figure 3. Evolution of the Dirac cone at  $K = (\frac{1}{3}, \frac{1}{3})$  as a function of  $\ell$ . The white dashed lines are calculations using the fitted LSWT Hamiltonian, while the background colormap shows experimental neutron scattering data. The two columns show perpendicular cuts through the  $K$  point. As  $\ell$  goes from 1 to 2, the cone flattens and inverts, such that the intensity at  $\ell = 1$  is opposite of  $\ell = 2$ . The two LSWT bands are degenerate at  $K$  throughout this evolution, yielding a nodal line. Note the emergence of a nodal plane at  $\ell = 1.5$ , where the two magnon bands degenerate everywhere in the  $hk$  plane.

of the physical layers, effectively breaking periodicity). The result is shown in Fig. 4 for 20 Gd unit cells (40 triangular lattice layers). LSWT [Fig. 4(b)] shows the presence of a clear surface mode, emerging from the bulk modes projected into the 2D surface Brillouin zone. Since inelastic neutron scattering is not a surface probe we cannot resolve the same mode in the data, but nevertheless find qualitative agreement with the bulk modes [panel (a)].

These experiments and calculations were carried out on Gd, which has near-perfect isotropic Heisenberg exchange. However, because of the intrinsic connection between symmetry, degeneracy, and topology [13, 14, 59–61] similar topological features can be expected in more anisotropic ferromagnetic HCP metals such as Tb [62, 63], Dy [62, 64], and hexagonal Co [65]. (However, for Co one must consider the effects of itinerancy on the possible Dirac spectrum [66] and continuum scattering likely eliminates the observability of Dirac magnons in HCP Co [67, 68].) From a topological magnon perspective, it is particularly interesting to consider the addition of Dzyaloshinskii-Moriya (DM) exchange interaction

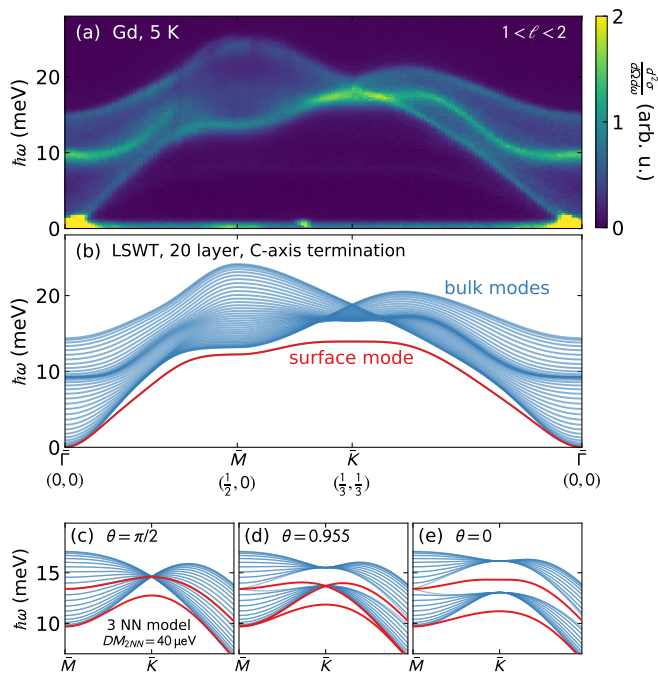


Figure 4. Surface magnons in Gd. (a) In-plane high-symmetry cuts of 5 K Gd scattering integrated from  $\ell = 1$  to  $\ell = 2$ . (b) Linear spin wave theory (LSWT) calculated modes for a 20-layer Gd slab using the best fit Hamiltonian. Note that, because of the finite extent along  $\hat{c}$ ,  $\ell$  is no longer a good quantum number, and the magnon modes from each layer form a continuum between  $\ell = 1$  and  $\ell = 2$ , such that the magnon modes strongly resemble the integrated data in panel (a). The  $c$ -axis termination surface magnon mode, shown in red, lies outside this continuum at lower energies, and is thus distinct from bulk magnons. Panels (c)-(e) show the bulk and surface modes with a 2nd neighbor DM of  $40 \mu\text{eV}$ , with ferromagnetic spin orientation at various angles  $\theta$  from the  $c$  axis. At  $\theta = 0.955$ , the surface modes cross, suggesting chiral surface magnons.

[69]

$$H = \sum_{ij} \mathbf{D} \cdot (\mathbf{S}_i \times \mathbf{S}_j), \quad (3)$$

where  $\mathbf{D}$  is the DM vector. Like on the honeycomb lattice [12], it is symmetry-allowed on the HCP lattice second nearest neighbor bonds. Although the superexchange mechanism considered by Moriya [69] may seem *prima facie* incompatible with the Ruderman-Kittel-Kasuya-Yosida (RKKY)-like magnetism in rare-earths like Gd [52], RKKY-mediated DM exchanges have, in fact, been discussed in other contexts [70–72], which leads us to speculate that weak DM exchanges may be possible also in spin-orbit-coupled rare-earths. A more concrete reason to consider DM exchange is that it may be relevant to other HCP ferromagnets, or to potential devices where the interfacial DM exchange can be strong due to breaking of inversion symmetry.

It is easily shown on the level of LSWT that single-ion anisotropy preserves the extended degeneracies, whereas DM exchange lifts the  $K$ -point and nodal plane degeneracy while leaving a grid of  $\ell = 1/2$  nodal lines. Perhaps most inter-

esting, the addition of asymmetric DM exchange brings the possibility of field-tunable topology, with chiral magnon surface modes and a nodal plane that can be turned on and off with a magnetic field. An example of such field-tunability is shown in Fig. 4(c)-(e), where a particular spin orientation gives crossing surface modes. It has been shown in other lattices that such crossings are chiral surface modes [12, 73–75], indicating the possibility of chiral HCP edge magnons. This band crossing is only possible with a sufficiently strong DM exchange interaction; for Gd the threshold DM exchange is  $36 \mu\text{eV}$ . Although this is unrealistic for Gd because of its isotropy, an anisotropic HCP compound like Tb may have sufficiently strong DM for chiral surface modes. Assuming a similar exchange Hamiltonian to Gd and given a Tb spin wave bandwidth of  $3/5$  that of Gd [62], the minimum DM exchange strength would be  $21 \mu\text{eV}$ . Thus even away from the Heisenberg limit, the elemental HCP ferromagnets would be interesting to investigate as platforms for non-Hermitian magnon topology [33] and interaction-stabilized topological phases [9, 76].

In conclusion, we have shown that the magnetic excitation spectrum of elemental gadolinium contains nodal line and nodal plane degeneracies, which are directly visible in the experimental data. The nodal line around  $K$  shows anisotropic intensity characteristic of nontrivial topology, and Berry phase calculations confirm this to be so. These results have implications not just for Gd, but for all HCP ferromagnets, as the topological features are generic to the lattice. One speculative physical consequence of the nodal line topology is a field-tunable chiral surface mode which appears with sufficiently strong DM exchange interaction. Other consequences exist of the HCP topology may exist—particularly concerning the nodal plane—but these are left for future study.

## ACKNOWLEDGMENTS

It is our pleasure to acknowledge helpful discussions with Paul McClarty, Roderich Moessner, and Satoshi Okamoto. This research used resources at the Spallation Neutron Source, a DOE Office of Science User Facility operated by the Oak Ridge National Laboratory. The research by P.L. was supported by the Scientific Discovery through Advanced Computing (SciDAC) program funded by the US Department of Energy, Office of Science, Advanced Scientific Computing Research and Basic Energy Sciences, Division of Materials Sciences and Engineering. The work by SEN is supported by the Quantum Science Center (QSC), a National Quantum Information Science Research Center of the U.S. Department of Energy (DOE).

\* [scheieao@ornl.gov](mailto:scheieao@ornl.gov)  
† [laurell@utexas.edu](mailto:laurell@utexas.edu)

- [1] T. Wehling, A. M. Black-Schaffer, and A. V. Balatsky, *Advances in Physics* **63**, 1 (2014).
- [2] S. Banerjee, D. S. L. Abergel, H. Ågren, G. Aeppli, and A. V. Balatsky, *Journal of Physics: Condensed Matter* **32**, 405603 (2020).
- [3] A. H. Castro Neto, F. Guinea, N. M. R. Peres, K. S. Novoselov, and A. K. Geim, *Rev. Mod. Phys.* **81**, 109 (2009).
- [4] F. Li, X. Huang, J. Lu, J. Ma, and Z. Liu, *Nature Physics* **14**, 10.1038/nphys4275 (2018).
- [5] A. B. Khanikaev, S. H. Mousavi, W.-K. Tse, M. Kargarian, A. H. MacDonald, and G. Shvets, *Nat. Mater.* **12**, 233 (2013).
- [6] L. Lu, Z. Wang, D. Ye, L. Ran, L. Fu, J. D. Joannopoulos, and M. Soljačić, *Science* **349**, 622 (2015), <https://science.sciencemag.org/content/349/6248/622.full.pdf>.
- [7] J. Fransson, A. M. Black-Schaffer, and A. V. Balatsky, *Phys. Rev. B* **94**, 075401 (2016).
- [8] S. Owerre, *Journal of Physics Communications* **1**, 025007 (2017).
- [9] S. S. Pershoguba, S. Banerjee, J. C. Lashley, J. Park, H. Ågren, G. Aeppli, and A. V. Balatsky, *Phys. Rev. X* **8**, 011010 (2018).
- [10] M. Malki and G. S. Uhrig, *EPL (Europhysics Letters)* **132**, 20003 (2020).
- [11] Z.-X. Li, Y. Cao, and P. Yan, *Physics Reports* **915**, 1 (2021).
- [12] P. McClarty, *arXiv preprint arXiv:2106.01430* (2021).
- [13] W. Brinkman, *Journal of Applied Physics* **38**, 939 (1967).
- [14] A. Corticelli, R. Moessner, and P. McClarty, *arXiv preprint arXiv:2103.05656* (2021).
- [15] K. Li, C. Li, J. Hu, Y. Li, and C. Fang, *Phys. Rev. Lett.* **119**, 247202 (2017).
- [16] F.-Y. Li, Y.-D. Li, Y. B. Kim, L. Balents, Y. Yu, and G. Chen, *Nature Communications* **7**, 12691 (2016).
- [17] A. Mook, J. Henk, and I. Mertig, *Phys. Rev. Lett.* **117**, 157204 (2016).
- [18] Y. Su, X. S. Wang, and X. R. Wang, *Phys. Rev. B* **95**, 224403 (2017).
- [19] Y. Su and X. R. Wang, *Phys. Rev. B* **96**, 104437 (2017).
- [20] L.-C. Zhang, Y. A. Onykiienko, P. M. Buhl, Y. V. Tymoshenko, P. Čermák, A. Schneidewind, J. R. Stewart, A. Henschel, M. Schmidt, S. Blügel, D. S. Inosov, and Y. Mokrousov, *Phys. Rev. Research* **2**, 013063 (2020).
- [21] A. Mook, J. Henk, and I. Mertig, *Phys. Rev. B* **95**, 014418 (2017).
- [22] S. Owerre, *Scientific reports* **7**, 1 (2017).
- [23] K. Hwang, N. Trivedi, and M. Randeria, *Phys. Rev. Lett.* **125**, 047203 (2020).
- [24] Y. Onose, T. Ideue, H. Katsura, Y. Shiomi, N. Nagaosa, and Y. Tokura, *Science* **329**, 297 (2010).
- [25] T. Ideue, Y. Onose, H. Katsura, Y. Shiomi, S. Ishiwata, N. Nagaosa, and Y. Tokura, *Phys. Rev. B* **85**, 134411 (2012).
- [26] M. Hirschberger, R. Chisnell, Y. S. Lee, and N. P. Ong, *Phys. Rev. Lett.* **115**, 106603 (2015).
- [27] R. Chisnell, J. S. Helton, D. E. Freedman, D. K. Singh, R. I. Bewley, D. G. Nocera, and Y. S. Lee, *Phys. Rev. Lett.* **115**, 147201 (2015).
- [28] R. Chisnell, J. S. Helton, D. E. Freedman, D. K. Singh, F. Demmel, C. Stock, D. G. Nocera, and Y. S. Lee, *Phys. Rev. B* **93**, 214403 (2016).
- [29] P. Laurell and G. A. Fiete, *Phys. Rev. B* **98**, 094419 (2018).
- [30] L. Chen, J.-H. Chung, B. Gao, T. Chen, M. B. Stone, A. I. Kolesnikov, Q. Huang, and P. Dai, *Phys. Rev. X* **8**, 041028 (2018).
- [31] B. Yuan, I. Khait, G.-J. Shu, F. C. Chou, M. B. Stone, J. P. Clancy, A. Paramekanti, and Y.-J. Kim, *Phys. Rev. X* **10**, 011062 (2020).
- [32] M. Elliot, P. A. McClarty, D. Prabhakaran, R. D. Johnson, H. C. Walker, P. Manuel, and R. Coldea, *Nature Communications* **12**, 1 (2021).
- [33] P. A. McClarty and J. G. Rau, *Phys. Rev. B* **100**, 100405 (2019).
- [34] S. Shivam, R. Coldea, R. Moessner, and P. McClarty, *arXiv preprint arXiv:1712.08535* (2017).
- [35] W. Yao, C. Li, L. Wang, S. Xue, Y. Dan, K. Iida, K. Kamazawa, K. Li, C. Fang, and Y. Li, *Nature Physics* **14**, 1011 (2018).
- [36] S. Bao, J. Wang, W. Wang, Z. Cai, S. Li, Z. Ma, D. Wang, K. Ran, Z.-Y. Dong, D. L. Abernathy, S.-L. Yu, X. Wan, J.-X. Li, and J. Wen, *Nature Communications* **9**, 2591 (2018).
- [37] H. E. Nigh, S. Legvold, and F. H. Spedding, *Phys. Rev.* **132**, 1092 (1963).
- [38] J. W. Cable and E. O. Wollan, *Phys. Rev.* **165**, 733 (1968).
- [39] G. Urbain, P. Weiss, and F. Trombe, *Comptes rendus* **200**, 2132 (1935).
- [40] R. M. Moon, W. C. Koehler, J. W. Cable, and H. R. Child, *Phys. Rev. B* **5**, 997 (1972).
- [41] A. F. Kip, *Rev. Mod. Phys.* **25**, 229 (1953).
- [42] S. Abdelouahed and M. Alouani, *Phys. Rev. B* **79**, 054406 (2009).
- [43] J. J. M. Franse and R. Gersdorf, *Phys. Rev. Lett.* **45**, 50 (1980).
- [44] W. C. Koehler, H. R. Child, R. M. Nicklow, H. G. Smith, R. M. Moon, and J. W. Cable, *Phys. Rev. Lett.* **24**, 16 (1970).
- [45] J. W. Cable, R. M. Nicklow, and N. Wakabayashi, *Phys. Rev. B* **32**, 1710 (1985).
- [46] J. W. Cable and R. M. Nicklow, *Phys. Rev. B* **39**, 11732 (1989).
- [47] G. E. Granroth, A. I. Kolesnikov, T. E. Sherline, J. P. Clancy, K. A. Ross, J. P. C. Ruff, B. D. Gaulin, and S. E. Nagler, *Journal of Physics: Conference Series* **251**, 012058 (2010).
- [48] G. E. Granroth, D. H. Vandergriff, and S. E. Nagler, *Physica B: Condensed Matter* **385-86**, 1104 (2006).
- [49] T. E. Mason, D. Abernathy, I. Anderson, J. Ankner, T. Egami, G. Ehlers, A. Ekkebus, G. Granroth, M. Hagen, K. Herwig, J. Hodges, C. Hoffmann, C. Horak, L. Horton, F. Klose, J. Larese, A. Mesecar, D. Myles, J. Neufeind, M. Ohl, C. Tulk, X.-L. Wang, and J. Zhao, *Physica B: Condensed Matter* **385**, 955 (2006).
- [50] O. Arnold, J. Bilheux, J. Borreguero, A. Buts, S. Campbell, L. Chapon, M. Doucet, N. Draper, R. Ferraz Leal, M. Gigg, V. Lynch, A. Markvardsen, D. Mikkelsen, R. Mikkelsen, R. Miller, K. Palmen, P. Parker, G. Passos, T. Perring, P. Peterson, S. Ren, M. Reuter, A. Savici, J. Taylor, R. Taylor, R. Tolchenov, W. Zhou, and J. Zikovsky, *Nuclear Instruments and Methods in Physics Research Section A: Accelerators, Spectrometers, Detectors and Associated Equipment* **764**, 156 (2014).
- [51] See Supplemental Material at [URL will be inserted by publisher] for more details of the experiments and calculations.
- [52] A. Scheie, P. Laurell, G. Granroth, M. B. Stone, and S. E. Nagler, *arXiv preprint arXiv:2107.11370* (2021).
- [53] C. Hwang, C.-H. Park, D. A. Siegel, A. V. Fedorov, S. G. Louie, and A. Lanzara, *Phys. Rev. B* **84**, 125422 (2011).
- [54] T. Holstein and H. Primakoff, *Phys. Rev.* **58**, 1098 (1940).
- [55] J. Jensen and A. Mackintosh, *Rare Earth Magnetism, Structures and Excitations* (Clarendon Press, Oxford, UK, 1991).
- [56] M. Xiao, L. Ye, C. Qiu, H. He, Z. Liu, and S. Fan, *Science advances* **6**, eaav2360 (2020).
- [57] W. Wu, Y. Liu, S. Li, C. Zhong, Z.-M. Yu, X.-L. Sheng, Y. X. Zhao, and S. A. Yang, *Phys. Rev. B* **97**, 115125 (2018).
- [58] S. Toth and B. Lake, *Journal of Physics: Condensed Matter* **27**, 166002 (2015).
- [59] A. P. Cracknell, *J. Phys. C: Solid State Phys.* **3**, S175 (1970).

- [60] P. Narang, C. A. C. Garcia, and C. Felser, *Nature Materials* **20**, 293 (2021).
- [61] H. Watanabe, H. C. Po, and A. Vishwanath, *Science Advances* **4**, 10.1126/sciadv.aat8685 (2018), <https://advances.sciencemag.org/content/4/8/eaat8685.full.pdf>.
- [62] P.-A. Lindgård, *Phys. Rev. B* **17**, 2348 (1978).
- [63] H. B. Møller, J. C. G. Houmann, and A. R. Mackintosh, *Journal of Applied Physics* **39**, 807 (1968).
- [64] R. M. Nicklow, N. Wakabayashi, M. K. Wilkinson, and R. E. Reed, *Phys. Rev. Lett.* **26**, 140 (1971).
- [65] T. Perring, A. Taylor, and G. Squires, *Physica B: Condensed Matter* **213**, 348 (1995).
- [66] S.-H. Do, K. Kaneko, R. Kajimoto, K. Kamazawa, M. B. Stone, S. Itoh, T. Masuda, G. D. Samolyuk, E. Dagotto, W. R. Meier, B. C. Sales, H. Miao, and A. D. Christianson, *arXiv preprint arXiv:2107.08915* (2021).
- [67] H. Okumura, K. Sato, and T. Kotani, *Phys. Rev. B* **100**, 054419 (2019).
- [68] T. Skovhus and T. Olsen, *Phys. Rev. B* **103**, 245110 (2021).
- [69] T. Moriya, *Phys. Rev.* **120**, 91 (1960).
- [70] D. Smith, *Journal of Magnetism and Magnetic Materials* **1**, 214 (1976).
- [71] A. Fert and P. M. Levy, *Phys. Rev. Lett.* **44**, 1538 (1980).
- [72] M. Schmitt, P. Moras, G. Bihlmayer, R. Cotsakis, M. Vogt, J. Kemmer, A. Belabbes, P. M. Sheverdyaeva, A. K. Kundu, C. Carbone, S. Blügel, and M. Bode, *Nature Communications* **10**, 1 (2019).
- [73] L. Zhang, J. Ren, J.-S. Wang, and B. Li, *Phys. Rev. B* **87**, 144101 (2013).
- [74] A. Mook, J. Henk, and I. Mertig, *Phys. Rev. B* **90**, 024412 (2014).
- [75] B. Li and A. A. Kovalev, *Phys. Rev. B* **97**, 174413 (2018).
- [76] A. Mook, K. Plekhanov, J. Klinovaja, and D. Loss, *Phys. Rev. X* **11**, 021061 (2021).

**SUPPLEMENTAL MATERIAL FOR “DIRAC MAGNONS,  
NODAL LINES, AND NODAL PLANE IN ELEMENTAL  
GADOLINIUM”**

**I. EXPERIMENT PARAMETERS**

For the SEQUOIA measurement, we ran the  $T0$  chopper at 90 Hz, Fermi 1 chopper at 120 Hz, Fermi 2 chopper at 360 Hz for  $E_i = 50$  meV. For  $E_i = 100$  meV we ran the same configuration but Fermi 2 chopper at 540 Hz. The sample was rotated in one degree steps to measure the inelastic spectra, and the data were reduced and symmetrized [50] to fill out the full Brillouin zone.

**II. SPIN-WAVE THEORY OF THE  $J_1 - J_2 - J_3 - J_4$  MODEL**

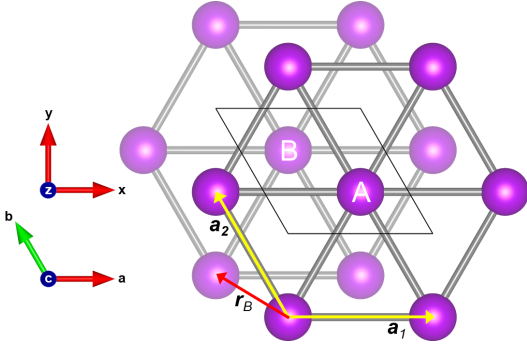


Figure S1. HCP crystal structure of Gd, with layers of triangular lattices. The two sublattices are labeled  $A, B$ . Both the crystallographic ( $abc$ ) and Cartesian ( $xyz$ ) coordinate systems are indicated, along with in-plane lattice vectors  $\mathbf{a}_{1/2}$  and basis vector  $\mathbf{r}_B$ . The vertical lattice vector,  $\mathbf{a}_3$ , points out of the depicted plane.

Here we provide analytical LSWT results for the simplified model. Although we limited the discussion in the main text to a  $J_1 - J_2 - J_3$  model, it is straightforward to include also  $J_4$  in the LSWT calculations, and we will do so here by considering

$$H = \sum_{n=1}^4 \sum_{i,j} J_n^{i,j} \mathbf{S}_i \cdot \mathbf{S}_j, \quad (\text{S1})$$

where  $J_n^{i,j} = J_n$  if sites  $i, j$  are  $n$ th nearest neighbors, and  $J_n^{i,j} = 0$  otherwise. Similarly to Ref. [55], we describe Gd as a two-sublattice ferromagnet consisting of ABAB-stacked triangular lattice layers, as shown in Fig. S1. Denoting the in- and out-of-plane lattice constants by  $a$  and  $c$ , respectively, the lattice ( $\mathbf{a}_i, i = 1, 2, 3$ ) and basis vectors ( $\mathbf{r}_{A/B}$ ) can be chosen (expressed in the  $(xyz)$  coordinate system indicated in Fig. S1)

$$\mathbf{a}_1 = (a, 0, 0), \quad \mathbf{a}_2 = \left( -\frac{a}{2}, \frac{a\sqrt{3}}{2}, 0 \right), \quad \mathbf{a}_3 = (0, 0, c), \quad (\text{S2})$$

$$\mathbf{r}_A = (0, 0, 0), \quad \mathbf{r}_B = \left( \frac{-a}{2}, \frac{a}{2\sqrt{3}}, \frac{c}{2} \right). \quad (\text{S3})$$

The resulting reciprocal lattice vectors are

$$\mathbf{b}_1 = \frac{2\pi}{a} \left( 1, \frac{1}{\sqrt{3}}, 0 \right), \quad \mathbf{b}_2 = \frac{4\pi}{a\sqrt{3}} (0, 1, 0), \quad (\text{S4})$$

$$\mathbf{b}_3 = \frac{2\pi}{c} (0, 0, 1). \quad (\text{S5})$$

To lowest order in the Holstein-Primakoff expansion,

$$S_i^+ = \sqrt{2S} a_i, \quad S_i^- = \sqrt{2S} a_i^\dagger, \quad S_i^z = S - a_i^\dagger a_i, \quad (\text{S6})$$

for  $i \in A$ , and with  $a_i \rightarrow b_i$  for  $i \in B$ . After substitution into Eq. (S1), keeping terms quadratic in creation and annihilation operators, and Fourier transforming we obtain the LSWT Hamiltonian

$$H^{(2)} = \sum_{\mathbf{k}} \left\{ C_d(\mathbf{k}) (a_{\mathbf{k}}^\dagger a_{\mathbf{k}} + b_{\mathbf{k}}^\dagger b_{\mathbf{k}}) + C_o(\mathbf{k}) a_{\mathbf{k}}^\dagger b_{\mathbf{k}} + C_o(-\mathbf{k}) b_{\mathbf{k}}^\dagger a_{\mathbf{k}} \right\}, \quad (\text{S7})$$

where

$$C_d(\mathbf{k}) = 12J_2S (\gamma_2(\mathbf{k}) - 1) + 4J_4S (\gamma_4(\mathbf{k}) - 1) - 12J_1S - 12J_3S - 2DS, \quad (\text{S8})$$

$$C_o(\mathbf{k}) = 12S [J_1\gamma_1(\mathbf{k}) + J_3\gamma_3(\mathbf{k})], \quad (\text{S9})$$

$\gamma_n(\mathbf{k}) = \frac{1}{z_n} \sum_{\vec{\delta}_n} e^{-i\mathbf{k} \cdot \vec{\delta}_n}$ ,  $z_n$  is the number of  $n$ th nearest neighbors, and  $\vec{\delta}_n$  are the  $n$ th nearest neighbor vectors. Explicitly, the neighbor vectors are given by

$$\vec{\delta}_1 \in \{ \mathbf{r}_B, \mathbf{a}_1 + \mathbf{r}_B, -\mathbf{a}_2 + \mathbf{r}_B, \mathbf{r}_B - \mathbf{a}_3, \mathbf{a}_1 + \mathbf{r}_B - \mathbf{a}_3, -\mathbf{a}_2 + \mathbf{r}_B - \mathbf{a}_3 \}, \quad (\text{S10})$$

$$\vec{\delta}_2 \in \pm \{ \mathbf{a}_1, \mathbf{a}_2, \mathbf{a}_1 + \mathbf{a}_2 \}, \quad (\text{S11})$$

$$\vec{\delta}_3 \in \{ \mathbf{a}_1 + \mathbf{a}_2 + \mathbf{r}_B, \mathbf{a}_1 - \mathbf{a}_2 + \mathbf{r}_B, -\mathbf{a}_1 - \mathbf{a}_2 + \mathbf{r}_B, \mathbf{a}_1 + \mathbf{a}_2 + \mathbf{r}_B - \mathbf{a}_3, \mathbf{a}_1 - \mathbf{a}_2 + \mathbf{r}_B - \mathbf{a}_3, -\mathbf{a}_1 - \mathbf{a}_2 + \mathbf{r}_B - \mathbf{a}_3 \}, \quad (\text{S12})$$

$$\vec{\delta}_4 \in \pm \mathbf{a}_3. \quad (\text{S13})$$

Note that HCP lattice sites are not centers of inversion, and that the  $\vec{\delta}_{1/3}$  vectors connect sublattices in the direction  $A \rightarrow B$ . (For  $B \rightarrow A$ , simply use  $\vec{\delta}_{1/3}^* = -\vec{\delta}_{1/3}$ .) With these vectors we obtain

$$\gamma_2(\mathbf{k}) = \frac{1}{3} \left[ \cos(ak_x) + 2 \cos\left(\frac{ak_x}{2}\right) \cos\left(\frac{\sqrt{3}ak_y}{2}\right) \right], \quad (\text{S14})$$

$$\gamma_4(\mathbf{k}) = \cos(ck_z), \quad (\text{S15})$$

both of which are manifestly real-valued, and

$$\gamma_1 = \frac{1}{6} \left( 1 + e^{ick_z} \right) \left( e^{\frac{iak_x}{2}} + e^{\frac{1}{2}ia(2k_x + \sqrt{3}k_y)} + e^{\frac{1}{2}i\sqrt{3}ak_y} \right) \times e^{-\frac{1}{6}i(3ck_z + 3ak_x + 2\sqrt{3}ak_y)}, \quad (\text{S16})$$

$$\gamma_3 = \frac{1}{6} \left( 1 + e^{ick_z} \right) \left( e^{2iak_x} + e^{ia(k_x + \sqrt{3}k_y)} + 1 \right) \times e^{-\frac{1}{6}i(3ck_z + 6ak_x + 2\sqrt{3}ak_y)}. \quad (\text{S17})$$

which are generally complex-valued. These functions all satisfy  $\gamma_n(-\mathbf{k}) = \gamma_n^*(\mathbf{k})$ , where  $*$  denotes complex conjugate. While  $\gamma_{2,4}(\mathbf{k})$  are invariant under both  $C_3$  and  $C_6$  rotations about  $\hat{k}_z$ ,  $\gamma_{1,3}(\mathbf{k})$  [and thus also  $h(\mathbf{k})$ ] only have  $C_3$  symmetry.

They are also invariant under  $C_3$  rotations about  $\hat{k}_z$ ,

Since there are no anomalous terms in the magnon Hamiltonian  $H^{(2)}$ , it can be diagonalized unitarily. We write

$$H^{(2)} = \text{const} + \sum_{\mathbf{k}} \mathbf{X}_{\mathbf{k}}^\dagger h(\mathbf{k}) \mathbf{X}_{\mathbf{k}}, \quad (\text{S18})$$

where

$$\mathbf{X}_{\mathbf{k}} = (a_{\mathbf{k}}, b_{\mathbf{k}})^T, \quad h(\mathbf{k}) = \begin{pmatrix} C_d(\mathbf{k}) & C_o(\mathbf{k}) \\ C_o^*(\mathbf{k}) & C_d(\mathbf{k}) \end{pmatrix}, \quad (\text{S19})$$

and diagonalize  $h(\mathbf{k})$ . This yields eigenvalues

$$\epsilon_{1,2} = -2S(6J_1 + 6J_2 + 6J_3 + 2J_4) + 12J_2S\gamma_2(\mathbf{k}) + 4J_4S\gamma_4(\mathbf{k}) \mp 12S|J_1\gamma_1(\mathbf{k}) + J_3\gamma_3(\mathbf{k})|, \quad (\text{S20})$$

with  $- (+)$  for  $\epsilon_1$  ( $\epsilon_2$ ), and eigenvectors

$$\psi_{1/2} = \frac{1}{\sqrt{2}} (\mp f(\mathbf{k}), +1)^T, \quad (\text{S21})$$

where

$$f(\mathbf{k}) = \frac{J_1\gamma_1(\mathbf{k}) + J_3\gamma_3(\mathbf{k})}{|J_1\gamma_1(\mathbf{k}) + J_3\gamma_3(\mathbf{k})|} \equiv \frac{g(\mathbf{k})}{|g(\mathbf{k})|}. \quad (\text{S22})$$

The gap  $2\Delta\epsilon(\mathbf{k}) = \epsilon_2(\mathbf{k}) - \epsilon_1(\mathbf{k}) = 24S|J_1\gamma_1(\mathbf{k}) + J_3\gamma_3(\mathbf{k})| = 24S|g(\mathbf{k})|$  only depends on the inter-sublattice interactions  $J_{1,3}$ . Non-accidental degeneracies occur when  $\gamma_1(\mathbf{k}) = \gamma_3(\mathbf{k}) = 0$ . The structure of Eqs. (S16), (S17) is such that this occurs either when the first factor vanishes,  $(1 + e^{ick_z}) = 0$ , or when the second factors vanish. At  $k_z = \pm\pi/c$  ( $\ell = \pm 1/2$ ),  $(1 + e^{ick_z}) = 0 \forall k_x, k_y$ , which produces the nodal planes. The second factors vanish at the  $K, K'$  points (which are related by a  $C_6$  rotation), and along paths  $K \rightarrow H \rightarrow K, K' \rightarrow H' \rightarrow K'$  at finite  $k_z$ , giving rise to the nodal lines.

As mentioned in the main text, the nodal lines can be classified in terms of a closed-path Berry phase,

$$\gamma_m[C] = \oint_C d\mathbf{k} \cdot \mathcal{A}_m(\mathbf{k}), \quad (\text{S23})$$

where  $C$  is a closed contour,  $\mathcal{A}$  is the Berry connection,

$$\mathcal{A}_m = i \langle u_m(\mathbf{k}) | \nabla_{\mathbf{k}} | u_m(\mathbf{k}) \rangle, \quad (\text{S24})$$

and  $|u_m(\mathbf{k})\rangle$  is an eigenstate of  $h(\mathbf{k})$ . Using Eq. (S21),

$$\mathcal{A} = \mathcal{A}_m = \frac{i}{2} f^*(\mathbf{k}) \nabla_{\mathbf{k}} f(\mathbf{k}), \quad \forall m, \quad (\text{S25})$$

from which it is clear that the topological properties are related to the intersublattice couplings  $J_{1,3}$ , and independent of  $J_{2,4}$ . (Thus the  $J_1, J_2, J_3$  model considered in the main text has

Table I. Berry phase calculated at loops surrounding different lines in momentum space. The leftmost column indicates a line segment, the  $\mathbf{k}$ -space coordinates of which are given in two coordinate systems (columns two and three).

Point	$(k_x, k_y, k_z)$	$(hk\ell)$	$\gamma_1 = \gamma_2$
$\Gamma - A - \Gamma$	$(0, 0, k_z)$	$(0, 0, \ell)$	0
$K - H - K$	$(\frac{2\pi}{3a}, \frac{2\pi}{\sqrt{3}a}, k_z)$	$(\frac{1}{3}, \frac{1}{3}, \ell)$	$\pi$
$K - H - K$	$(-\frac{4\pi}{3a}, 0, k_z)$	$(-\frac{2}{3}, \frac{1}{3}, \ell)$	$\pi$
$K - H - K$	$(\frac{2\pi}{3a}, -\frac{2\pi}{\sqrt{3}a}, k_z)$	$(\frac{1}{3}, -\frac{2}{3}, \ell)$	$\pi$
$K' - H' - K'$	$(-\frac{2\pi}{3a}, -\frac{2\pi}{\sqrt{3}a}, k_z)$	$(-\frac{1}{3}, -\frac{1}{3}, \ell)$	$-\pi$
$K' - H' - K'$	$(\frac{4\pi}{3a}, 0, k_z)$	$(\frac{2}{3}, -\frac{1}{3}, \ell)$	$-\pi$
$K' - H' - K'$	$(-\frac{2\pi}{3a}, \frac{2\pi}{\sqrt{3}a}, k_z)$	$(-\frac{1}{3}, \frac{2}{3}, \ell)$	$-\pi$

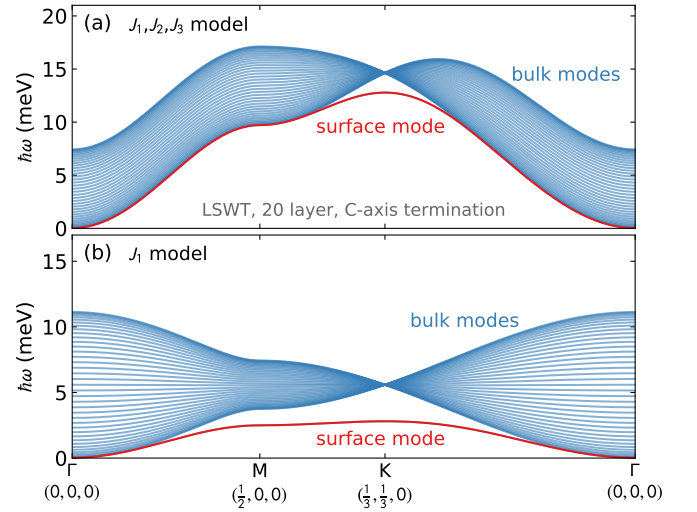


Figure S2. Surface magnons for a simplified Linear spin wave theory (LSWT) models, showing the topological band crossings and surface modes are independent of the particular model details. (a) Surface magnon calculated for a 20-layer Gd slab using the three nearest neighbor fitted exchange interactions. (b) Surface magnon calculated for the nearest neighbor exchange only. Note that in both cases, the bulk modes linearly cross at  $K$ , while the surface magnon mode lies outside this continuum, indicating that this surface magnon is a property of the lattice symmetry rather than the details of the Hamiltonian.

identical topology to the model here.) To obtain  $\gamma_m$ , it is convenient to shift the  $\mathbf{k}$ -space origin to e.g.  $K$ , using coordinates  $(k'_x, k'_y, k'_z)$  and then introduce cylindrical coordinates,

$$k'_x = \rho \cos \varphi, \quad k'_y = \rho \sin \varphi, \quad k'_z = k_z. \quad (\text{S26})$$

such that  $\rho$  describes the radius of a circular loop about the nodal line, and  $\varphi$  the angle along the loop. Then direct evaluation of Eq. (S25) (here performed using Mathematica at various  $k_z$  values) yields  $\gamma = \pm\pi$  at  $K$  and  $K'$ , see Table I.

As noted in the main text, the nodal line gives rise to a clear topological surface mode. The degree to which it separates from the bulk modes does depend on the specific exchanges



included in the Hamiltonian. This is illustrated by the results for a pure  $J_1$  model and the  $J_1-J_2-J_3$  model shown in Fig. S2,

using the same slab geometry supercell as for the full fitted model.